Journal of Korean Magnetics Society, Volume 5, Number 5, October 1995

SLIDERS FOR THE NEXT GENERATION MAGNETIC HARD DISK DRIVE SYSTEMS-NUMERICAL SIMULATION

Myung S. Jhon*, Paul R. Peck*, Soo-Choon Kang, and Benjamin L. Wang***
* Department of Chemical Engineering, ** Department of Mechanical Engineering
Carnegie Mellon University, Pittsburgh, PA, 15213, USA

In-Eung Kim and Ki-Ook Park
Magnetic Storage Lab., Samsung Advanced Institute of Technology, Suwon, 440-600, Korea

Abstract-Fundamental issues and general procedures of modeling the head disk interface (HDI) in order to provide design criteria for future ultra-low flying sliders are given. Intermittent contact and gaseous rarefaction effects are discussed using nonconventional kinetic theory. To illustrate the simulation results, we modeled IBM 3370 taper flat sliders and positive/negative "bow tie" sliders. Several alternative HDI concepts for future disk drives - viscoelastic bearings, a hybrid system, and contact recording - are also briefly discussed.

I .INTRODUCTION

The main goal in the disk drive industry is to develop a reliable, low cost, and high density storage device. The efforts to achieve this goal will continue into the next decade as shown in Figure 1, and the Data Storage Systems Center at Carnegie Mellon University is pursuing the development of a 10 Gigabits per square inch hard disk drive system. Note that 10 Gigabits represents the memory required to store five million double-spaced typed pages, which is approximately comparable to a stack of papers having a height of a 150 story building. These ultra-high densities will necessitate lower flying heights, improved tribochemical characteristics (carbon overcoats, lubricants, etc.), in addition to improved recording heads (e.g., magnetoresistive head), media (e.g., barium ferrite without carbon overcoat [1]), signal processing, and track following.

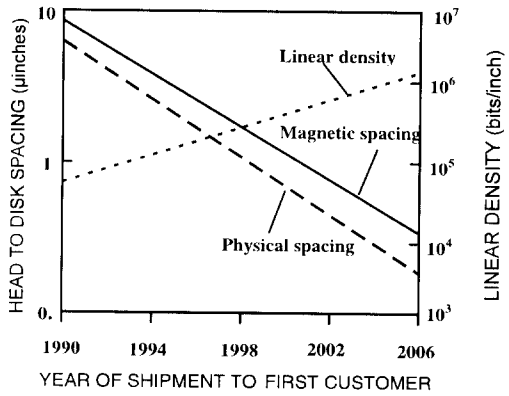

Figure 1 Storage density growth during the past and next decades [2]

In this paper, we exclusively focus our attention on the technology associated with flying height reduction. We will discuss the necessary technology in order to achieve ½ - 2 μinches (50nm) flying height, even though the ultimate goal is contact recording (almost zero spacing between the head and media which is analogous to tape or floppy drives). As the flying height is drastically reduced to achieve ultra-high density, severe interaction between the head and disk results. This interaction can lead to significant wear of the disk surface which may cause catastrophic loss of data. This may also be important in removable hard disk drive systems where transient particles momentarily disturb the air bearing which increases the head-disk spacing.

This paper describes several essential features of mathematical modeling needed to advance ultra-low flying and pseudo-contact recording technologies. We will focus on the miniaturization and transient dynamics of an IBM 3370 taper flat slider and symmetrical and asymmetrical "bow tie" shaped rail sliders, with cuts on the inside and outside edges of the slider rails. Miniaturization decreases material costs as well as the overall cost of the device. Smaller masses and faster rotational speeds also result in lower power consumption and latency of recording, respectively. Smaller disks and recording heads facilitate higher storage through both smaller head-disk separation (i.e. lower flying height), which increases the areal density of stored information, and through tighter stacking of disks within the head-disk assembly, which increases the volumetric density of the device.

We will study gaseous rarefaction effects using kinetic theory and we will also investigate surface roughness effects. Viscoelastic bearings, hybrid models combining air and liquid bearings, and contact recording technology will be briefly discussed.

II.GENERAL PHILOSOPHY OF HEAD DISK INTERFACE (HDI) MODELING

The general methodology used in HDI simulations is as follows: (i) for a given slider geometry and disk topography, calculate the pressure distribution beneath the slider rails using an appropriate governing equation, and (ii) from the pressure distribution, determine the orientation and location of the slider as a function of time. For pseudo-

contact recording, intermittent contact between the slider and disk occurs and additional information regarding the frequency and magnitude of these collisions should be incorporated into simulations. Everybody has their own favorite method of developing simulation code, however, none of the HDI simulations reported in the literature can be reliably applied to the design of ultra-low flying sliders including intermittent contact.

Numerical simulation of the HDI involves two sets of governing equations, one which determines the motion of the slider suspension and another which determines the pressure distribution between the slider rails and the disk. The slider suspension is usually modeled using linear springs and dashpots, yielding the rigid body equations of motion that govern the location and orientation of the slider;

$$m\frac{d^2z}{dt^2}+c_z\frac{dz}{dt}+k_zz+F=\iint(p-p_a)dA+q\delta(t-t^*)\,. \tag{1}$$

$$\begin{aligned} I_\theta\frac{d^2\theta}{dt^2}+c_\theta\frac{d\theta}{dt}+k_\theta\theta+(k_zz+F)(x_{cg}-x_{pp}) &= \iint(p-p_a)(x_{cg}-x)dA \\ &+\iint\left(\frac{h}{2}\frac{\partial p}{\partial x}-\frac{\mu U_x}{h+2\alpha\lambda}\right)z_{cg}dA \\ &+q\delta(t-t^*)\{(x_{cg}-x^*)+\varsigma z_{pp}\}\,, \end{aligned} \tag{2}$$

$$\begin{aligned} I_\phi\frac{d^2\phi}{dt^2}+c_\phi\frac{d\phi}{dt}+k_\phi\phi+(k_zz+F)(y_{pp}-y_{cg}) &= \iint(p-p_a)(y-y_{cg})dA \\ &+\iint\left(\frac{\mu U_y}{h+2\alpha\lambda}-\frac{h}{2}\frac{\partial p}{\partial y}\right)z_{cg}dA+q\delta(t-t^*)(y^*-y_{cg})\,. \end{aligned} \tag{3}$$

In Eqs. (1) - (3), z, θ, and φ are the vertical displacement, pitch angle, and roll angle of the slider relative to its initial static attitude (z_e, θ_e, and ϕ_e); x_{cg}, y_{cg}, and z_{cg} are the location of the center of gravity; x_{pp}, y_{pp}, and z_{pp} are the location of the load point of the slider; m is the mass of the slider; I_θ and I_ϕ are the moments of inertia; k_z, k_θ, and k_ϕ are suspension stiffness coefficients; c_z, c_θ, and c_ϕ are suspension damping coefficients; F is the normal load; and p and p_a are the bearing and ambient pressures respectively. A schematic illustration of these variables is given in Figure 2. The additional terms appearing in Eqs. (1) - (3) account for air bearing shear stresses along the bottom of the slider rails (the integral term) and slider disk collisions. Some simulation codes do not include these terms, and provide incorrect values for the pitch and roll angles. Wall shear stress contributions depend on the viscosity (μ) and mean free path (λ) of the gas, the relative disk velocity in both the x and y directions (U_x and U_y), the flying height (h), as well as the surface accommodation factor (α). Slider-disk collisions, which are assumed to be impulsive (simplest model) and are represented by the Dirac delta function δ, occur at time t^* and at the location x^* and y^*. The relative contribution of slider-disk collisions to the dynamic motion of the slider assembly will depend on their magnitude (q) as well as the kinetic coefficient of friction (ζ) between the surface of the slider and disk. Standard numerical integration procedures (e.g., Runge-Kutta, predictor-corrector, etc.) are used to solve the ordinary differential equations given in Eqs. (1) - (3).

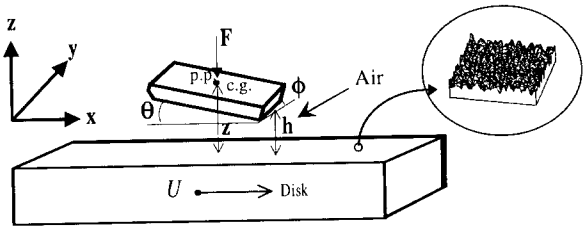

Figure 2. Schematic of a typical head-disk interface.

The equation governing the pressure distribution, p(x,y), between the slider and disk surface is conveniently written in the following generalized Reynolds equation form, and is solved using the finite element method (FEM)

$$\begin{aligned} &\frac{\partial}{\partial x}\left(ph^3Q_r\frac{\partial p}{\partial x}\right)+\frac{\partial}{\partial y}\left(ph^3Q_r\frac{\partial p}{\partial y}\right) \\ &=6\mu U_x\frac{\partial(ph)}{\partial x}+6\mu U_y\frac{\partial(ph)}{\partial y}+12\mu\frac{\partial(ph)}{\partial t}\,. \end{aligned} \tag{4}$$

In Eq. (4), Q_r accounts for modifications due to gaseous rarefaction effects and is usually referred to as the total mass flow rate coefficient. Q_r will be extensively discussed below.

III. GASEOUS RAREFACTION EFFECTS AND DEVELOPMENT OF NEW KINETIC THEORY

In the past, the gas between the surfaces of the slider and disk was considered as a continuum. Gaseous rarefaction effects were first incorporated into HDI models by Burgdorfer [3] who introduced first-order slip flow boundary conditions. In his analysis, Burgdorfer expressed slip flow as a truncated Taylor expansion in both the mean free path of the gas and the tangential stress at the wall. Hsia and Domoto [4] extended the analysis to include second-order slip flow effects. Direct expansion of Burgdorfer's method to higher order rarefaction effects is conceptually difficult in continuum mechanics, since the velocity profile v(x,y,z) between the surface of the slider and disk is quadratic (i.e., $\partial^n v/\partial x^n = 0$ for $n > 2$).

Numerous authors [5] - [8] have included higher ordered rarefaction effects by deriving equations based upon the linearized Boltzmann equation (LBE). The only approximation of the LBE adopted for HDI simulations incorporated the Bhatnagar-Gross-Krook's (BGK) approximation [9]. A major numerical drawback of formulations which are based upon the Boltzmann equation, is that the complex integrals accounting for molecular collisions must be evaluated during each numerical iteration. Fukui and Kaneko [8] attempted to alleviate this problem by predetermining the values of these integrals for a wide range Knudsen numbers (Kn = λ/h). Integration within each iteration was thereby replaced by a database search procedure. Several attempts to fit Fukui and Kaneko's database of Q_r values have been reported [10, 11]. The most accurate single equation analytic fit of Boltzmann results was obtained using a Padé form (or continued fraction formulation),

$$Q_r = 1 + 6Kn\frac{\left(a_{c,Kn=0}-1\right)\left(\alpha'+\sqrt{\beta'}\right)+\left(a_{c,Kn=\infty}-1\right)\sqrt{\varepsilon' Kn}}{\alpha'+\sqrt{\beta'+\varepsilon' Kn}}, \qquad (5)$$

where $a_c = (Q_r - 1)/6Kn$. Equation (5) replicated database values of Q_r over the entire range of Knudsen numbers given, using only three independent parameters which were determined using a Monte-Carlo best fit procedure. This equation also gives the correct asymptotic limiting behavior for $Kn \to 0$ and $Kn \to \infty$, i.e.,

$$\begin{aligned} a_c(Kn \to 0) &= \frac{2.0324}{\sqrt{\pi}} + \frac{4.2612}{\pi} Kn \cdots, \\ a_c(Kn \to \infty) &= 4.473 - \frac{12.059}{\sqrt{Kn}} + \frac{17.366}{Kn} \cdots. \end{aligned} \qquad (6)$$

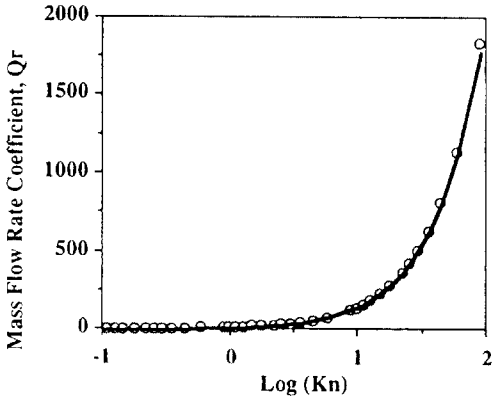

Figure 3 Database values (denoted as circles) of the total mass flow rate coefficient, Q_r, and the numerical fit (line) obtained from Eqs. (5) and (6). $\alpha' = 3.849$, $\beta' = 0.33536$, $\varepsilon' = 0.63269$.

Under ultra-low flying conditions, molecule-surface collisions occur more often than molecule-molecule collisions. The Boltzmann equation discussed above, which assumes chaotic molecular collisions, is invalid under ultra-low flying conditions. A rigorous kinetic equation is currently being developed, which is structurally similar to the Fokker-Planck equation [12, 13]. In this paper, however, we will only compare the mathematical structures of the Boltzmann equation (with the BGK approximation), an alternative kinetic equation (the Fokker-Planck equation), and the collisionless kinetic equation.

The first time derivative of a one particle distribution function, $f(\boldsymbol{r},\zeta,t)$, is described by the following kinetic equation (using dimensionless velocity, $\zeta = v/v_0$, where v is the molecular velocity and $v_0 = (k_bT/m)^{1/2}$ is the thermal velocity of the gas [12, 13])

$$\left(\frac{\partial}{\partial t} + v_0\zeta\cdot\frac{\partial}{\partial \boldsymbol{r}}\right) f(\boldsymbol{r},\zeta,t) = A(f). \qquad (7)$$

A(f) contains the collisional information of the gas molecules and depends on the kinetic model chosen. The LBE/BGK model (B) yields

$$\begin{aligned} A_B(f) &= -f(\boldsymbol{r},\zeta,t) \\ &\quad + \varphi(\zeta)\int d^3\zeta'\left[1+\zeta\cdot\zeta'+1/6\left(\zeta^2-3\right)\left(\zeta'^2-3\right)\right] f(\boldsymbol{r},\zeta',t), \end{aligned} \qquad (8)$$

while the Fokker-Planck model (FP) yields [12, 13]

$$\begin{aligned} A_{FP}(f) &= \frac{\partial}{\partial\zeta}\cdot\left(\zeta+\frac{\partial}{\partial\zeta}\right) f(\boldsymbol{r},\zeta,t) \\ &\quad + \varphi(\zeta)\int d^3\zeta'\left[\zeta\cdot\zeta'+1/3\left(\zeta^2-3\right)\left(\zeta'^2-3\right)\right] f(\boldsymbol{r},\zeta',t), \end{aligned} \qquad (9)$$

where $\varphi(\zeta) = (2\pi)^{-3/2}\exp(-\zeta^2/2)$ is the dimensionless Maxwell-Boltzmann distribution function. The collisionless kinetic equation (C) yields

$$A_C(f) = 0. \qquad (10)$$

All of the collision terms A(f) satisfy the conservation laws of number, momenta, and energy, respectively,

$$\int d^3\zeta \begin{Bmatrix} 1 \\ \zeta \\ \zeta^2 \end{Bmatrix} (A_B \text{ or } A_{FP} \text{ or } A_C) = 0. \qquad (11)$$

To compare the three different collision terms (B, FP, and C), we expand A(f) in terms of the generalized Hermite polynomial tensors $H^{(n)}_{i_1,i_2,\cdots,i_n}(\zeta)$ [12,13],

$$A(f) = \int d^3\zeta'\Xi(\zeta,\zeta')\, f(\boldsymbol{r},\zeta',t), \qquad (12)$$

with $\Xi(\varsigma,\varsigma') = \sum_n \lambda_n \varphi(\varsigma) H^{(n)}_{i_1,\cdots,i_n}(\varsigma) H^{(n)}_{i_1,\cdots,i_n}(\varsigma')$.

Here, $H^{(n)}_{i_1,\cdots,i_n}(\varsigma) = \frac{(-1)^n}{\varphi(\varsigma)} \frac{\partial}{\partial \varsigma_{i_1}} \cdots \frac{\partial}{\partial \varsigma_{i_n}} \varphi(\varsigma)$.

Noting that $H^{(n)}_{i_1,\cdots,i_n}(\varsigma)$ are the eigenfunctions of the Fokker-Planck operator [12,13], that is

$$\frac{\partial}{\partial \varsigma}\left(\frac{\partial}{\partial \varsigma} + \varsigma\right) \varphi(\varsigma) H^{(n)}_{i_1,\cdots,i_n}(\varsigma) = -n\varphi(\varsigma) H^{(n)}_{i_1,\cdots,i_n}(\varsigma) , \qquad (13)$$

we can obtain the eigenvalues λ_n. λ_n for the three models and the range of application of the equations are qualitatively summarized in Figure 4. Note that all of the models satisfy conservation laws, implying five zero eigenvalues (see Eq. (11)).

The best kinetic theory descriptive for ultra-low flying is the Fokker-Planck like equation, however, we may choose an average between the LBE/BGK and collisionless kinetic models as a good approximation. The calculation of Q_f based on rigorous kinetic theory is currently under investigation.

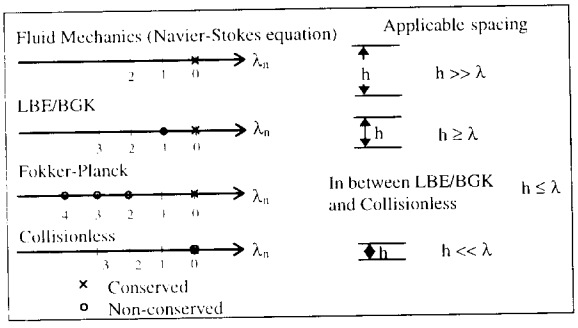

Figure 4 Eigenvalues for the three different kinetic models and illustration of the applicable spacing ranges.

IV. ULTRA-LOW FLYING SLIDERS AND MINIATURIZATION CRITERIA

In order to calculate the ultra-low flying characteristics of sliders, several numerical methods are utilized to solve Eqs. (1) - (5) simultaneously. A finite element method algorithm, based on an element by element approach [14, 15], solves the time dependent generalized Reynolds equation iteratively with the force and moment balances. The non-linearity of Eq. (4) is handled by using a modified Newton-Rhapson scheme, and the resulting equations are solved using a bi-conjugate gradient method [16]. Eqs. (1) - (3) are solved using a fourth order Runge-Kutta method. All of the rarefaction models described and arbitrary roughness or surface configuration are also incorporated to the current numerical algorithm.

Sharp pressure gradients due to surface roughness or height discontinuities can cause numerical instabilities in many algorithms. A flux corrected transport scheme is used to alleviate this problem. This scheme decreases numerical instabilities while maintaining accuracy. Further, we added a fast Fourier transform algorithm to aid in interpreting HDI experiments. The dynamic simulation algorithm is capable of solving transient responses of sliders but usually needs a great amount of computing time to obtain steady state results. Another algorithm has been developed to obtain the steady state flying orientation within a few minutes. This code is based on the conventional finite element method which assembles the global stiffness matrix and uses a direct matrix solver. State-of-the-art graph theory is incorporated to minimize the bandwidth of the global stiffness matrix and higher order elements are used to handle discontinuities which make solutions unstable around sharp edges.

Numerical simulations were performed for steady state and dynamic transient analysis. Steady state simulations incorporated various slider geometries and miniaturization effects. The miniaturization results are used to obtain a scaling theory [17]. This theory is based on an order of magnitude approximation to the load bearing capacity definition and the equation of motion. A form of the equation is,

$$h^2 + A' \frac{a_c R_f}{\sqrt{FP_{amb}}} h + B' \frac{UR_f^3}{F} = 0 , \qquad (14)$$

where h is the trailing edge flying height, F is the normal load applied to the slider, U is the linear disk velocity, and R_f is a percent reduction factor of a given slider size (i.e., R_f = 0.5 corresponds to a 50% nano slider). The effective surface accommodation factor a_c accounts for gaseous rarefaction effects and depends on the generalized Reynolds equation chosen. The two constants A′ and B′ are determined using two results from numerical simulations, and Eq. (14) gives excellent agreement with simulation results for IBM 3370 taper flat sliders over a wide range of operating conditions. This scaling theory is very useful in estimating the steady state film thickness for numerical simulations, which aids in reducing computational efforts. Figure 5 shows steady state simulation results of the trailing edge flying height and pitch angle for several miniaturized sizes (full, micro, nano, and pico) of an IBM 3370 taper flat slider with a normal load of 5 grams and a linear disk velocity of 21.5 m/sec.

To validate the scaling theory, the air bearing surface geometry was altered and a "bow tie" shaped air bearing surface shown in Figure 6 was developed. The area of the air bearing surface and the length and width of the slider are consistent with an IBM 3370 slider for comparison purposes. This "bow tie" slider shape is chosen to reflect the current industrial trend of adopting negative pressure sliders with

complex air bearing surfaces (e.g., Seagate negative pressure sliders or Guppy slider). These designs employ hour glass shaped side rails to achieve stable ultra-low flying heights.

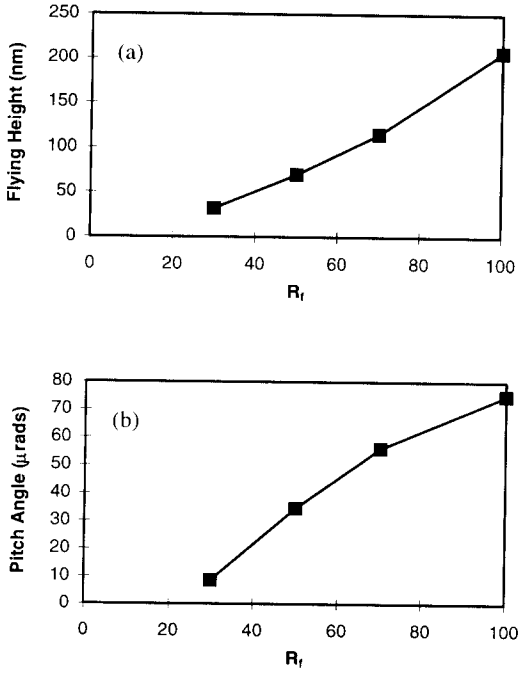

Figure 5 FEM results of an IBM 3370 taper flat slider:
(a) Flying height versus percent reduction factor (R_f)
(b) Pitch angle versus percent reduction factor (R_f)

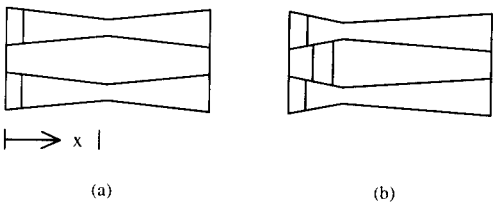

Figure 6 Geometry of "bow tie" sliders: (a) positive and (b) negative (x indicates the percentage of the slider length as measured from the leading edge)

The location of the hour glass neck (x) is considered as a design variable. The numerical results for the trailing edge flying height and pitch angle are shown in Figure 7 as a function of x. A 100% "bow tie" slider is used in simulations with a 1 gram normal load and 10 m/sec disk velocity. Figure 8 shows the influence of the hour glass neck on the pressure distribution between the leading edge and trailing edge region. The pitch angle depends on this pressure balance, and the variations of the flying height at the trailing edge are altered by this angle.

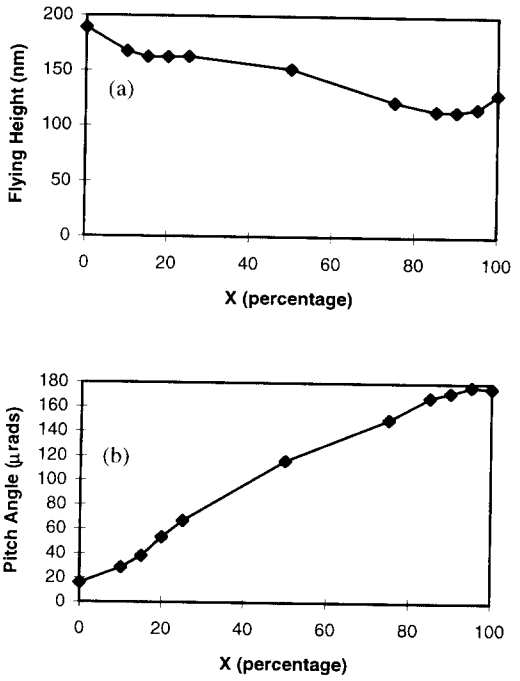

Figure 7. Effect of the location of the neck for a "bow tie" slider:
(a) Flying height at the trailing edge versus the location of the neck (x)
(b) Pitch angle versus the location of the neck (x)

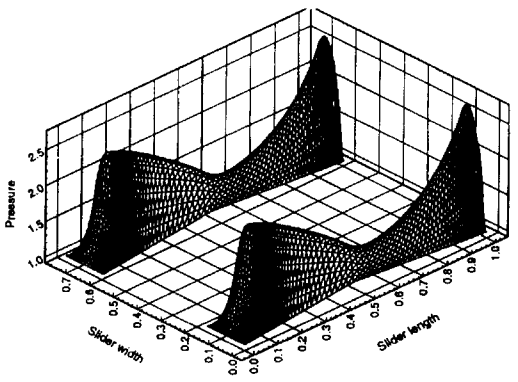

Figure 8 Steady state dimensionless pressure profile for a 100% "bow tie" slider with x = 50% of slider length

Miniaturization effects of "bow tie" sliders with x = 50% of the slider length (we refer to this as a symmetric "bow tie") are shown in Figure 9.

Journal of Korean Magnetics Society, Volume 5, Number 5, October 1995

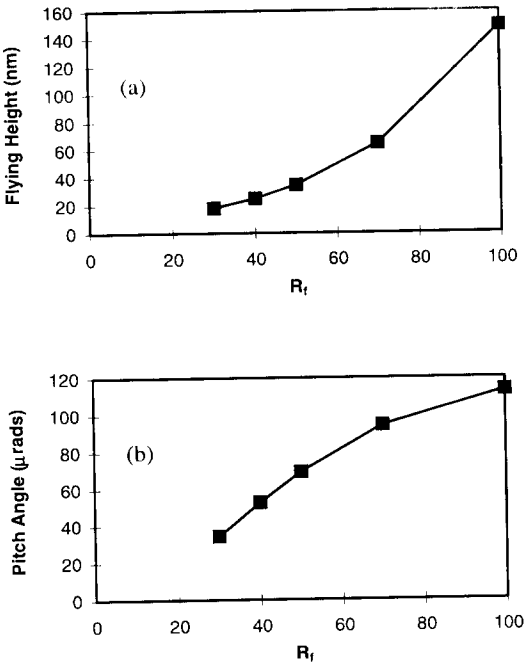

Figure 9 FEM results of a symmetric "bow tie" slider
(a) Flying height versus percent reduction factor (R_f)
(b) Pitch angle versus percent reduction factor (R_f)

In addition to steady state simulations, dynamic transient simulations were also performed to explore flying characteristic over contaminated surfaces. Figure 10 shows the trailing edge flying height and pitch angle response for a 100% negative "bow tie" slider which has one cross rail connecting the two side "bow tie" rails to generate a negative pressure region. This negative pressure generates a suction force which draws the slider towards the disk and reduces the flying height drastically. The slider is initially dropped from 100nm with a 1 gram applied normal load and a 10 m/sec disk velocity. The damping of oscillations in order to minimize head to disk contacts is an important phenomena, especially as the flying height is reduced. The flying height in this case is 90 nm, although experimental flying height measurements for this geometry are not readily available for verification of the results.

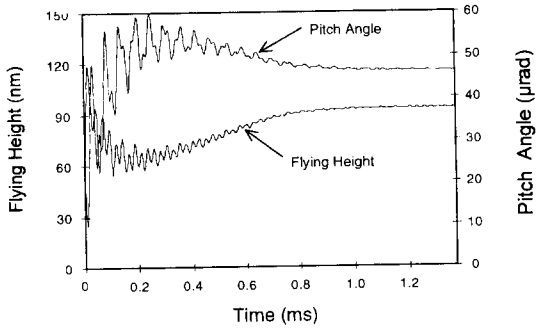

Figure 10 Initial transient response of a negative "bow tie" slider

Other simulations were performed to analyze the transient dynamics of sliders passing over asperities located at the disk surface (moving roughness). Figure 11 shows the pressure contour beneath the negative "bow tie" slider rails while passing over an asperity. Figure 12 shows the transient response of a slider passing over an ellipsoidal asperity 200 μm in diameter, 50 nm in height, and centered over the outer rail.

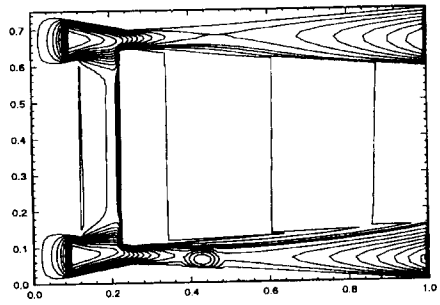

Figure 11 Pressure contour beneath a negative "bow tie" slider (x = 25 %) while passing over an ellipsoidal asperity

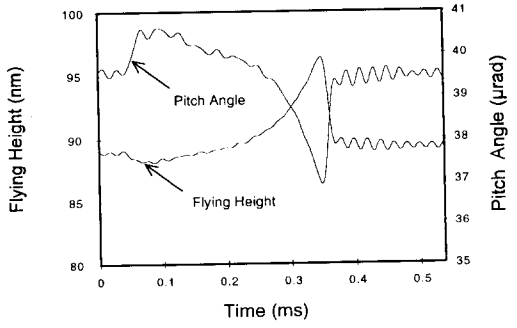

Figure 12 Transient response of a negative "bow tie" slider (x = 25 %) passing over an ellipsoidal asperity.

V.DISCUSSION AND CONCLUSIONS

In this paper, several fundamental features of modeling the HDI in order to formulate design criteria for future ultra-low flying recording heads were examined. The modeling of state-of-the-art air bearing simulations was described, which includes the Boltzmann equation descriptive for gaseous rarefaction of current slider designs and the finite element method. For future sliders flying under 1 μinch (25 nm), two issues should be considered. One is the problem of intermittent contacts. The simplest model is the incorporation of the delta function terms in Eqs. (1) - (3). The other issue is the adoption of an accurate gaseous rarefaction model. More sophisticated theory is needed to replace the Boltzmann type. A couple of kinetic equations (Fokker-Planck and collisionless equations) were discussed as possible replacements of the Boltzmann/BGK model. Calculation of Q_r from the new kinetic equation may require complicated algebraic details. One quick remedy is to modify Eqs. (5)-(6) for any kinetic equation developed. The limiting values, $a_{c,kn=0}$ and $a_{c,kn\to\infty}$ in Eq. (5), can be replaced by analytic solutions obtained from any arbitrary kinetic theory one chooses.

To illustrate simulation results, we miniaturized IBM 3370 taper flat sliders. A scaling law was tested based on these results which has two parameters. These parameters are primarily dependent on the shape of the slider. To test the scaling theory further we developed "bow tie" positive and negative pressure sliders inspired by the Seagate negative pressure slider design. Scaling results for the "bow tie" sliders are given, as well as the transient slider dynamic behavior over well-defined asperities. The transient dynamic study over asperities and pits is very important in studying contaminated environments, especially for removable disk drive systems.

The recommendations given in this paper can be essential in developing slider design criteria for pseudo-contact recording air bearing technology. The methodology we provide here could also be important in studying the lift forces for contact recording sliders [18]. It is worthwhile to mention the interesting concept of viscoelastic liquid bearings (VLB), known commercially as VISqUS technology. In VLB, a viscoelastic liquid is used as the supporting layer instead of air [19]. Therefore, the mechanical performance of the disk drive will be primarily dependent on the rheological properties of the chosen fluid. In general, when a fluid is confined in a small geometry, the apparent viscosity not only depends on the shear rate, but also on the characteristic length of the confined geometry [19, 20]. The analysis reported in this paper can easily be extended to VLB technology as long as we have physically realistic rheological equations of state for the fluid in the confined geometry.

Finally, new HDI designs combining air and liquid bearings - we call them "hybrid" systems - are very challenging to model. This system can be made by using a reasonably thicker lubricant layer without carbon overcoat (for example, lubricant layer over barium ferrite media [1]). Design criteria for sliders used in this "hybrid" interface are challenging to calculate even though the analysis we reported here can be generalized to this system. Our analysis should incorporate a complex two-phase fluid model in order to simulate an accurate pressure profile.

REFERENCES

[1] M. Scherge, C. L. Bauer, M. S. Jhon, X. Sui, and M. Kryder, "Tribological Properties of Barium Ferrite," IEEE Trans. Magn. (submitted).

[2] J. L. Simonds, Physics Today, April 1995, p.26.

[3] A. Burgdorfer, ASME J. Basic Eng., **81**, 94 (1959).

[4] Y.-T. Hsia and G. A. Domoto, ASME J. Lub. Tech., **105**, 120 (1983).

[5] R. M. Crone, Ph.D. Thesis, Carnegie Mellon University (1992).

[6] R. F. Gans, ASME J. Trib., **107**, 431 (1985).

[7] S. Fukui and R. Kaneko, ASME J. Trib., **110**, 253 (1988).

[8] S. Fukui and R. Kaneko, ASME J. Trib., **112**, 78 (1990).

[9] P. F. Bhatnagar, E. P. Gross, and M. Krook, Phys. Rev., **94**, 511 (1954).

[10] O. J. Ruiz and D.B. Bogy, ASME J. Trib., **112**, 593 (1990); O. J. Ruiz and D.B. Bogy, ASME J. Trib., **112**, 603 (1990).

[11] R. M. Crone, M. S. Jhon, T. E. Karis, and B. Bhushan, Adv. Info. Storage Syst., **4**, 105 (1992).

[12] M. S. Jhon and D. Forster, Phys. Rev., **A12**, 254 (1975); M. S. Jhon and J. S. Dahler, J. Chem. Phys., **74**, 279, (1981).

[13] S. Yip and S. Ranganthan, Phys. Fluids., **8**, 1956 (1965).

[14] R. M. Crone, M. S. Jhon, B. Bhushan, and T. E. Karis, Adv. Info. Storage Syst., **1**, 189 (1991).

[15] R. M. Crone, M. S. Jhon, T. E. Karis, and B. Bhushan, Adv. Info. Storage Syst., **3**, 15 (1991).

[16] H. A. van der Vorst, SIAM J. Sci. Stat. Comput., **13**, 631 (1992).

[17] R. M. Crone, P. R. Peck, M. S. Jhon, and T. E. Karis, ASME J. Trib., **115**, 566 (1993).

[18] C. Foster, Data Storage, Jan./Feb. 1995, p.23.

[19] P. R. Peck, M. S. Jhon, R. F. Simmons, and T. J. Janstrom, Appl. Phys., **75**, 5747 (1994); P. R. Peck, H. J. Kim, M. S. Jhon, R. F. Simmons, and T. J. Janstrom, J. Mag. Soc. Japan, **18**(S1), 513 (1994).

[20] S. Granick, Science, **253**, 1374 (1991).